Fabrication, structural, optical, electrical, and humidity sensing characteristics of hierarchical NiO nanosheet/nanoball-flower-like structure films

N. Parimon[1,3] · M. H. Mamat[1,2] · I. B. Shameem Banu[4] · N. Vasimalai[4] · M. K. Ahmad[5] · A. B. Suriani[6] · A. Mohamed[6] · M. Rusop[1,2]

Abstract

In this work, nickel oxide (NiO) nanosheet/nanoball-flower-like structures (NSBS) were directly grown on a NiO seed-coated glass substrate using a low-temperature immersion method at 75 ºC. The thickness, or density, of the nanoball-flower-like structures differed based on the following samples order: NSBS1 < NSBS2 < NSBS3. The synthesised NSBS films were investigated in terms of structural, optical, electrical, and humidity sensing characteristics. The X-ray diffraction (XRD) analysis revealed that the NSBS samples corresponded to the face-centred cubic NiO with five diffraction patterns indexed to the (111), (200), (220), (311), and (222) planes. The interplanar spacing, lattice parameter, unit cell volume, strain, and stress were also determined from the XRD results. The transmittance spectra showed that the NSBS samples had a transparency of more than 30% in the visible region. The optical bandgap values for the NSBS samples were estimated in the range between 3.72 and 3.75 eV, which is directly related to their lattice expansion and defect characteristics. The current–voltage and Hall effect measurement results revealed that the NSBS2 displayed good electrical properties with the resistance, hole concentration, and hole mobility values of 7.84 MΩ, 8.71×10^{15} hole/cm^{-3}, and 1.88×10^2 cm^2/V s, respectively. The NSBS samples performed well for humidity sensing with the highest sensitivity value of 169 being obtained for the NSBS2. These humidity sensing results correlated well with their structural, optical, and electrical characteristics.

✉ M. H. Mamat
mhmamat@uitm.edu.my

✉ N. Vasimalai
vasimalai@crescent.education

1 NANO-ElecTronic Centre (NET), Faculty of Electrical Engineering, Universiti Teknologi MARA (UiTM), 40450 Shah Alam, Selangor, Malaysia

2 NANO-SciTech Centre (NST), Institute of Science (IOS), Universiti Teknologi MARA (UiTM), 40450 Shah Alam, Selangor, Malaysia

3 Faculty of Engineering, Universiti Malaysia Sabah (UMS), 88400 Kota Kinabalu, Sabah, Malaysia

4 School of Physical and Chemical Sciences, B.S. Abdur Rahman Crescent Institute of Science & Technology, Vandalur, Chennai 600 048, India

5 Microelectronic and Nanotechnology–Shamsuddin Research Centre (MiNT-SRC), Faculty of Electrical and Electronic Engineering, Universiti Tun Hussein Onn Malaysia (UTHM), 86400 Batu Pahat, Johor, Malaysia

6 Nanotechnology Research Centre, Faculty of Science and Mathematics, Universiti Pendidikan Sultan Idris (UPSI), 35900 Tanjung Malim, Perak, Malaysia

1 Introduction

Nickel oxide (NiO) is one of the transition metal oxides with a bandgap energy in a range between 3.6 and 4.0 eV. It is commonly known as a p-type semiconductor material due to the Ni-deficiency represented in the nonstoichiometric NiO, and its electrical conductivity is based on the hole as the carrier [1, 2]. Although a p-type semiconductor is rarely used as a preferred material for electronic device applications, it has become an alternative to n-type metal oxides in many applications. Due to the many attractive properties of NiO, it provides a huge potential for applications in solar cells [3–5], electrochemical energy storage devices [6, 7], photocatalysts [8], and sensors [9, 10].

To date, many NiO-based gas-related sensors can be referred to in the literature [11–13], while only a few reports on NiO-based humidity sensors are available. For instance, Ulhaq et al. fabricated Al-doped NiO ultralong nanowires using a hydrothermal method for ethanol sensing [9]. They measured the ethanol sensing performance at different humidity levels. According to their study, the maximum

sensitivity of the ethanol sensing was obtained at 45% RH with a value of 14. Singh et al. reported the performance of a ZnO–NiO heterostructure-based liquefied petroleum gas sensor that was prepared using a chemical co-precipitation method [14]. They measured the gas sensing at different humidity levels ranging from 20 to 60% RH and found that the response was reduced at higher humidity levels. Recent studies have shown that humidity sensors are still being developed for use in various fields, such as industrial and laboratory, agricultural, medical, and climatology for continuous monitoring of water vapour [15]. Therefore, a systematic study on the NiO nanostructures for humidity sensing applications is required to understand the nanostructure characteristics in terms of structural, optical, and electrical parameters that influence the humidity sensing performance. Furthermore, the characteristics of NiO nanostructures, and their performances in several applications, are still far from expected, probably due to their structural parameters and the substandard activity of the energetic sites in the NiO lattice. A good humidity sensor requires high stability and sensitivity where the sensing performance is strongly influenced by the high surface area and the porous structure [16]. Thus, a specific morphology with an enormous surface area is necessary to produce a large area of exposure to trap water molecules during humidity sensing activity. It will then provide more adsorption and desorption sites during the sensing process. Besides, the water molecules are easily adsorbed in open porous areas and cause water condensation within the capillary pores [15].

There are several ways to obtain unique and valuable NiO morphologies to improve the surface area and thus enhance the sensing performance. These approaches include a multiplicity of preparation methods by augmenting their growth parameters, surface engineering through physical and chemical techniques, and composite or doping processes [17–19]. In terms of the preparation method, solution-based approaches including electrochemical, hydrothermal, and solution immersion methods are very promising to produce NiO nanostructures with novel morphologies and characteristics [12, 13, 20]. Particularly, by using the solution immersion method, NiO nanostructures could be synthesised at a low cost with exciting outputs due to the characteristics of the method itself that is facile, and which does not require a complex and time-consuming process. Herein, in this work, we synthesised NiO nanosheet/nanoball-flower-like structures (NSBS) that were grown directly on a NiO seed layer-coated glass substrate using the low-temperature immersion method at 75 °C. The properties in terms of the structural, optical, electrical, and humidity sensing of NSBS were thoroughly studied. To the best of our knowledge, the preparation of the NSBS based on a low-temperature solution immersion method, and their characteristics in humidity sensing have been scarcely reported in the literature.

2 Experimental and characterisation

The synthesis of NSBS films involved two steps. The first step was the deposition of the NiO seed layer as a base surface (also known as NiO seed-coated) on top of a glass substrate using sol–gel spin coating. Initially, the microscope glass substrates were cut into 2.5 cm × 2.5 cm and cleaned in a mixture of hydrochloric acid and deionised (DI) water. Next, the substrates were rinsed with DI water. Subsequently, the substrates were cleaned separately using acetone, ethanol, and DI water in an ultrasonic bath (Hwasin Technology PowerSonic 405, 40 k Hz) for 15 min each. The cleansed glass substrates were blown dry using nitrogen gas. The solution of NiO seed layers was prepared using 0.2 M nickel acetate tetrahydrate ($Ni(CH_3COO)_2 \cdot 4H_2O$), diethanolamine (DEA, $C_4H_{11}NO_2$), and ethylene glycol monoethyl ether (EGMEE, $C_4H_{10}O_2$). The solution was prepared by mixing 0.2 M nickel acetate tetrahydrate and 2 ml DEA in a beaker before the EGMEE was added into the beaker to produce 50 ml solution. The prepared precursor solution was stirred for 2 h at room temperature. The solution was directly coated on the top of the glass substrates using a spin coater at the deposition speed of 4000 rpm for 1 min. After the coating, the film was pre-baked at 250 °C for 5 min. The coating and pre-bake processes were repeated five times to increase the seed layer thickness. Next, the seed layer film was annealed at 400 °C for 2 h.

The second step was the growth of NSBS by using the low-temperature immersion method. An aqueous solution consisting of 0.2 M nickel (II) nitrate hexahydrate ($Ni(NO_3)_2 \cdot 6H_2O$), 0.2 M hexamethylenetetramine ($C_6H_{12}N_4$), and deionised (DI) water as a precursor, stabiliser, and solvent, respectively, was prepared in a beaker to grow NSBS. The solution was sonicated using an ultrasonic bath for 30 min and was further stirred for 45 min at 300 rpm in ambient conditions. The solution was then poured into Schott bottles, where the NiO seed-coated glass substrates were placed at the bottom. The NiO-coated surface of the glass was placed facing up. The Schott bottles were immersed in a water bath instrument (Memmert) at 75 °C for different growth times, from 1 to 3 h, to vary the thickness and the nanoball-like-flower density in the NSBS films. Then, the samples were removed from the bottles and rinsed with DI water. Finally, the samples were dried in a furnace (Protherm) at 150 °C for 15 min and were annealed and 500 °C for 1 h. The samples grown for 1, 2, and 3 h were abbreviated as NSBS1, NSBS2, and NSBS3, respectively.

The NSBS samples were characterised using field emission scanning electron microscopy (FESEM, Zeiss Supra 40VP and Hitachi SU-8030) for the surface and

cross-sectional morphologies. The structural properties of the NSBS were investigated using X-ray diffraction (XRD, PANalytical X'Pert PRO). The optical properties of the NSBS were characterised using ultraviolet–visible (UV–vis) spectroscopy (Jasco/V-670 EX). The electrical properties of the NSBS samples were analysed using a two-probe current–voltage (I–V) measurement system (Advantest R6243) in the voltage range between − 10 and 10 V. The Hall effect measurements of the NSBS were conducted using a Hall effect measurement system (ezHEMS). The humidity sensing performances of the devices were analysed in a humidity chamber (ESPEC-SH261) with the measurement system (Keithley 2400). The schematic of humidity sensing measurement setup is depicted in Fig. 1. Prior to I–V, the Hall effect, and the humidity sensing measurements, silver (Ag) contacts were deposited on the NSBS samples as electrodes, using a thermal evaporation system (Ulvac VPC 1100) with the thickness fixed at 60 nm. The gap between the contacts was 2 mm.

3 Results and discussion

3.1 Field effect scanning electron microscopy analysis

Figure 2a–l shows the cross-sectional images and surface morphologies of the NSBS sample grown using the solution immersion method. The images show that at the low-immersion temperature of 75 °C, the NiO nanosheet and NiO nanoball-flower-like structures were well grown on the

NiO seed-coated glass substrates with a good coverage. It shows that the NiO seed layer successfully promoted the heterogenous growth of NiO nanostructures on the substrate and acted as a catalyst. The average thicknesses of the NSBS1, NSBS2, and NSBS3 were 8.80, 16.08, and 20.82 μm, respectively. The images in Figs. 2a–c, d–f, g–i, and j–l show the cross-sectional of the NSBS samples at a magnification of ×4000, cross-sectional of the NSBS samples at a magnification of ×10,000, a cross-sectional of the produced nanosheet in the NSBS films, and the surface morphologies of the NSBS samples, respectively.

The cross-sectional images at a magnification of ×4000 presented in Fig. 2a–c show that all samples consisted of NSBS. Dense and hierarchical nanoball-flower-like structures on the nanosheet layers can be clearly observed in the NSBS1–NSBS3. The nanoball-flower-like structures are well-formed on the substrates with a high density. The films of NSBS exhibit porous structures with the voids between the individual nanoball-flower-like structures clearly seen in the cross-sectional images. Meanwhile, the cross-sectional images at a larger magnification of ×10,000 are depicted in Fig. 2d–f. It is noteworthy that the nanoball-flower-like NiO in the NSBS1–NSBS3 samples have diameters varying between 1.5 and 3.3 μm. The petals of the nanoball-flower-like structures can be seen as being tremendously thin with a highly porous surface. It can also be observed that the nanoball-flower-like structures consist of multiple nanosheets that are assembled together, producing networks of NiO nanostructures with a high surface availability.

Figure 2g–i shows the nanosheet structures from the cross-sectional morphology of NSBS films. The nanosheets can be seen as grass-like shapes in an array

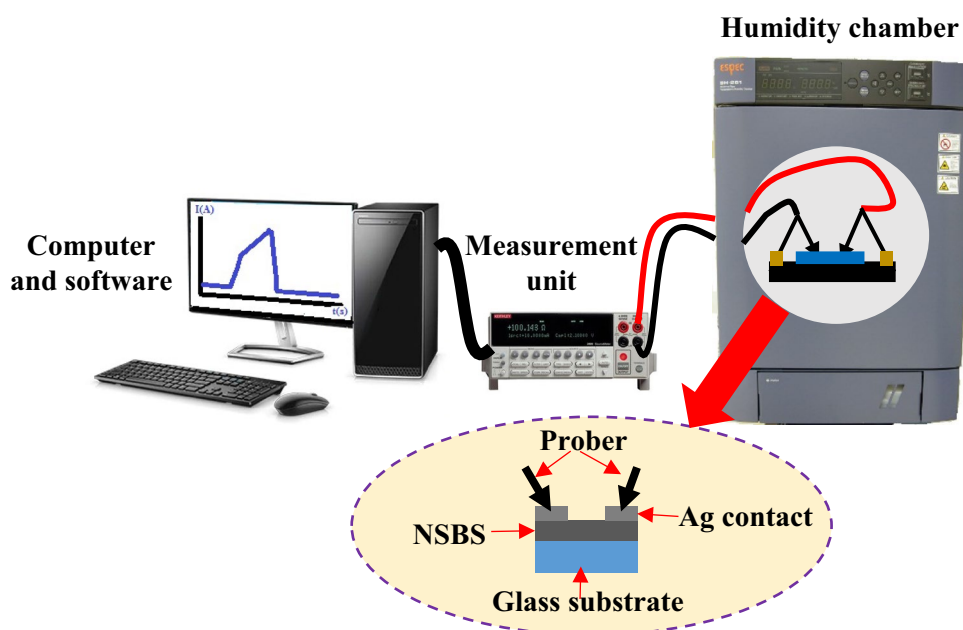**Fig. 1** Schematic of the humidity sensing measurement setup for NSBS samples

Fig. 2 Cross-sectional images of **a** NSBS1, **b** NSBS2, and **c** NSBS3 samples at a magnification of ×4000. Larger magnification of cross-sectional images at ×10,000 for **d** NSBS1, **e** NSBS2, and **f** NSBS3 samples. Cross-sectional images of NiO nanosheet structures on **g** NSBS1, **h** NSBS2, and **i** NSBS3 samples. Surface morphologies of **j** NSBS1, **k** NSBS2, and **l** NSBS3 samples
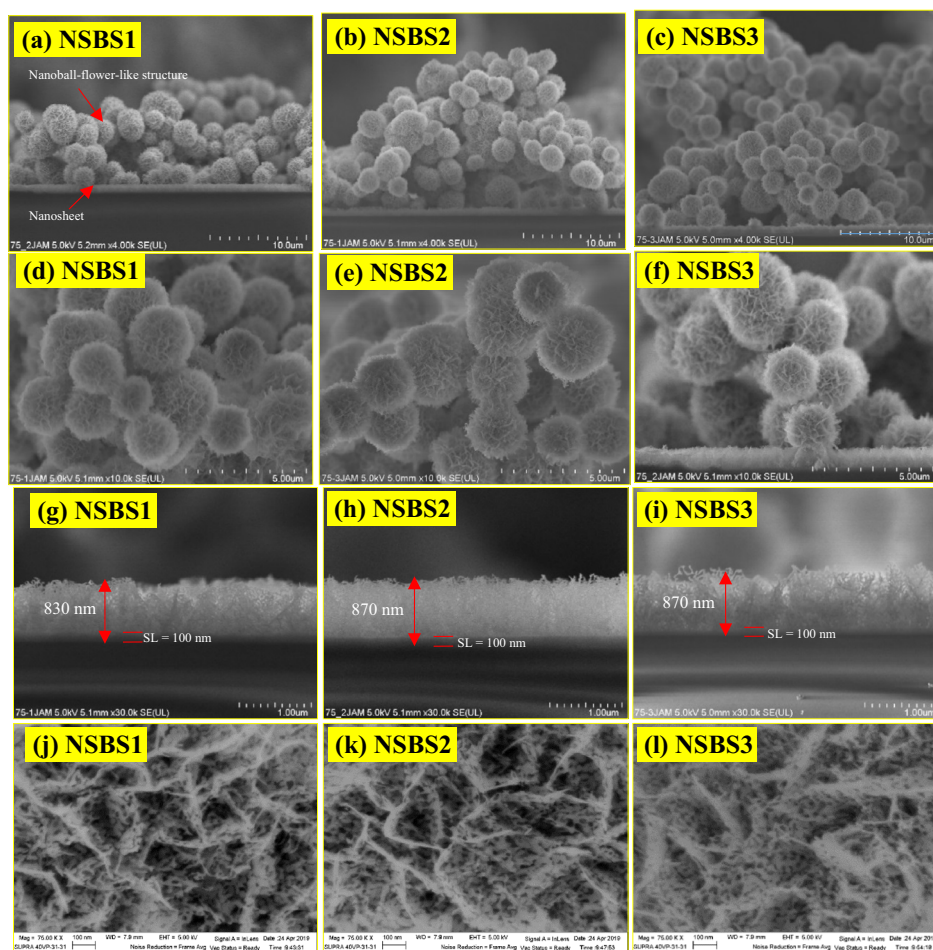
which grows evenly on the NiO seed layers for all samples. Among the three samples, the NSBS2 sample showed the densest and most well-structured growth. The thicknesses of the nanosheet array in the NSBS showed slight variations for different samples, which were 830 nm, 870 nm, and 870 nm for NSBS1, NSBS2, and NSBS3, respectively. Note that the NiO seed layer, which was deposited by a sol–gel spin-coating technique on a glass substrate, had a thickness of approximately 100 nm.

The surface morphologies of NSBS1, NSBS2, and NSBS3 are shown in Fig. 2j–l. The images show that the NSBS structures have highly porous and hollow structures. The images show that NSBS samples have a series of thin interconnected network structures consisting of small granular NiO nanoparticles. The NSBS networks exhibit a hollow structure with the presence of fine holes on the surface. The surface area of the NSBS is enormous and beneficial to the acceleration and greater adsorption of water molecules when exposed to humidity. In general, no significant changes were observed on the surface morphologies of NSBS for all samples. However, the petals

structure in the NSBS3 sample appears to be gradually decomposed, dispersed, and not sharp compared to the petal structures in NSBS1 and NSBS2.

The growth mechanism of NSBS can be proposed as follows. The HMT acts as a complex agent and favours the growth of NiO nanostructures by providing alkaline conditions [21–23]. In general, HMT can dissolve in DI water to release ammonia and formaldehyde. This reaction can be described by the equation below:
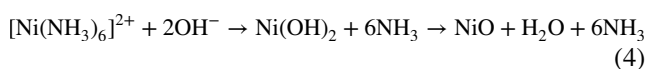
$$(CH_2)_6N_4 + 6H_2O \rightarrow 6HCHO + 4NH_3 \tag{1}$$

The Ni^{2+} ions, which are generated when the precursor dissolves in the water, react with the produced ammonia to form complex $[Ni(NH_3)_6]^{2+}$ ions. The presence of water molecules also facilitates the basic conditions by hydrolysis of NO_3^- ions from the precursor which stimulates the planar growth of NiO. The reaction between Ni^{2+} ions and ammonia decreases the concentration of the precursor's Ni^{2+} ions. As a result, the growth rate of the NiO crystal reduces in the solution. The overall reaction from this process can be expressed by the following equation:
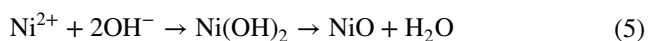
$$Ni(NO_3)_2 \cdot 6H_2O + 6NH_3 \rightarrow [Ni(NH_3)_6]^{2+} + 2NO_3^- + 6H_2O \quad (2)$$
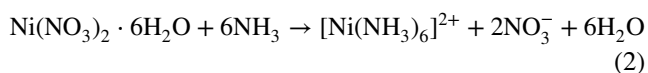
The ammonia also reacts with the water to produce NH^{4+} and OH^- ions. As the reaction proceeds, this reaction increases the concentration of OH^- ions in the solution. This reaction can be described as follows:

$$NH_3 + H_2O \rightarrow NH_4^+ + OH^- \quad (3)$$
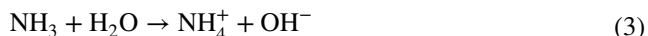
When the solution contains a sufficient OH^- ion concentration to reach supersaturation level, which exceeds its critical value, the NiO nuclei forms on the seed-catalyst layer based on the reaction between $[Ni(NH_3)_6]^{2+}$ and/or Ni^{2+} ions with OH^- ions. These reactions are shown as follows:

$$[Ni(NH_3)_6]^{2+} + 2OH^- \rightarrow Ni(OH)_2 + 6NH_3 \rightarrow NiO + H_2O + 6NH_3 \quad (4)$$

and/or

$$Ni^{2+} + 2OH^- \rightarrow Ni(OH)_2 \rightarrow NiO + H_2O \quad (5)$$

The morphology of the nanosheet on the substrate is controlled by the remaining HMT which has not reacted with the precursor's Ni^{2+} ions. These HMT molecules are adsorbed on certain plane orientations of NiO, predominantly on the (001) plane. As such, the growth of NiO is favourable to form a thin nanosheet structure [24]. The highly dense nanosheet structure, which grows perpendicular to the substrate, was firstly produced on the seed layer-coated glass due to the high concentration of precursor ions and HMT in the solution. Therefore, NiO nuclei form on the seed layer-coated glass with high density to initiate the formation of a highly dense NiO nanosheet. As the reactions proceed, the NiO nanoball-flower-like structure is formed on the dense NiO nanosheet. The NiO nanoball-flower-like structures are assembled from aggregated NiO nanoparticles, which act as seed catalysts to grow the structure into nanoball-flower-like structures. The nucleation of primary NiO nanoparticles is assisted by the hotspots created in the solution, which are considered as the starting reaction point in the solution [25]. These hotspots are formed through the heating of the precursor solution in the water bath. The HMT used in the precursor solution could also assist the formation of the hotspots in the solution. The HMT favours the nucleation of aggregated NiO nanoparticles and their subsequent growth into nanoball-flower-like structures. During the immersion process, the aggregation of NiO nanoparticles happens to reduce the free surface energy of the system. Note that the surface energy of the initial NiO nanoparticles is high and as such, they tend to aggregate to reduce the free surface energy. In a slow precipitation condition, the aggregation

of NiO nanoparticles happens along a crystal plane which forms a petal like morphology. Then, the produced petals randomly self-assemble before the nanoball-flower-like structure morphology is formed through the Ostwald ripening processes. The growth of the NSBS structure is also highly dependent on other parameters including temperature, hydrogen bonding, interactions of hydrophobic/hydrophilic, dipolar fields, forces (i.e. electrostatic and van der Walls), and attractions of crystal-faces [26]. The schematic for the growth of NSBS on the NiO seed layer-coated glass substrate is depicted in Fig. 3.

3.2 X-ray diffraction analysis

To investigate the structural quality of the NSBS1, NSBS2, and NSBS3 samples, XRD measurements were conducted. The XRD patterns in Fig. 4 indicate that all NSBS samples display polycrystalline structures that correspond to the face-centred cubic type of NiO, in accordance with JCPDS NO. 047-1049. The XRD patterns show three diffraction peaks with high intensities, which were indexed to the (111), (200), and (220) planes. Meanwhile, there are two nonprominent diffraction peaks in the XRD patterns which can be indexed to the (311) and (222) planes. It can be perceived that the peak at the (200) plane displayed the dominant intensity for all the NSBS samples. In addition, no other phase was identified from the XRD measurements which indicate that the polycrystalline NiO samples were well formed during the growth process. The higher intensity of the diffraction peaks of NSBS3 and NSBS2, compared to that of NSBS1, is attributed to the higher density NiO nanoball-flower-like structures grown on the substrates. Note that, the broad peak between 20º and 40º is attributed to the peak of the glass substrate used in this study [27, 28].

A detailed description of the crystal properties is summarised in Table 1. Among these values recorded are 2θ, intensity, full width at half maximum (FWHM), crystallite size (D), interplanar spacing (d), lattice parameter (a), unit cell volume (V), strain (ε'), and stress (σ). The crystal structure was evaluate based on the (200) plane orientation for all NSBS samples. The crystallite size (D) was estimated according to the Scherrer's formula:

$$D = \frac{0.94\lambda}{\beta \cos \theta} \quad (6)$$

where λ is the X-ray wavelength (1.542 Å), β is the FWHM in radians, and θ is the Bragg's angle of diffraction in degrees. The calculated crystallite size values of NSBS1, NSBS2, and NSBS3 were 16.62 nm, 16.58 nm, and 17.73 nm, respectively. The differences in crystallite size, lattice parameter, and strain properties may cause peak broadening in the XRD pattern [29]. It has been reported
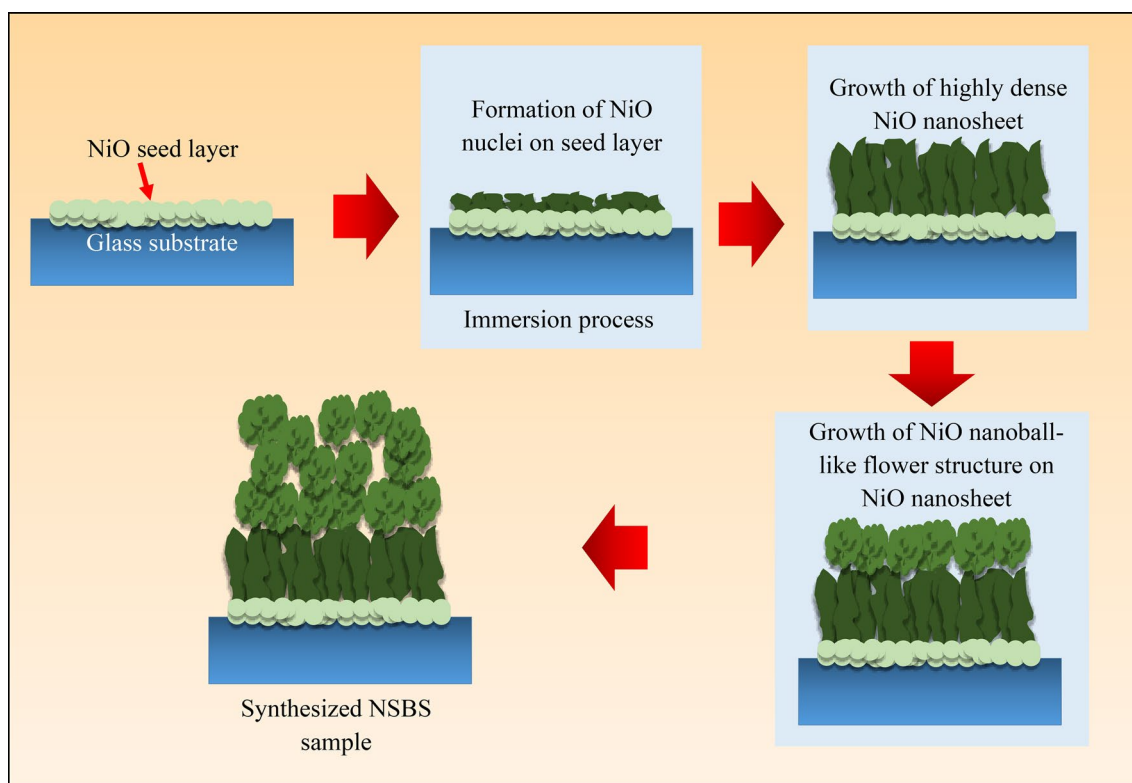
Fig. 3 The schematic for the growth of NSBS on the NiO seed layer-coated glass substrate
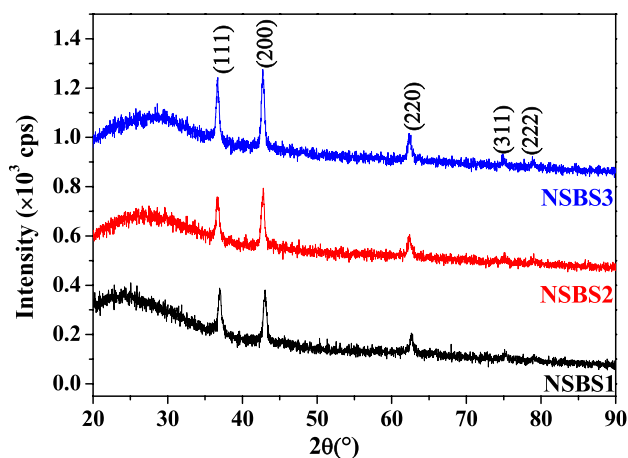

Fig. 4 The XRD pattern of NSBS samples

that the variation in crystallite size is due to the aggregation and recrystallization during the crystal growth processes including heat treatment [30, 31].

The interplanar spacing (*d*) and lattice parameter (*a*) of cubic NiO structure are estimated based on the following equations:

$$d = \frac{n\lambda}{2\sin\theta} \tag{7}$$

$$\frac{1}{d^2} = \frac{h^2 + k^2 + l^2}{a^2} \tag{8}$$

where $n = 1$ is the order value of diffraction, and *h*, *k*, and *l* are the Miller indices of the plane. The *d* and *a* values for NSBS1, NSBS2, and NSBS3 are tabulated in Table 1.

Table 1 2θ, FWHM, crystallite size, interplanar spacing, lattice parameter, unit cell volume, strain, and stress of NSBS1, NSBS2, and NSBS3 samples

Sample	2θ (°)	FWHM, β (°)	Crystallite size, D (nm)	Interplanar spacing, d (Åm)	Lattice parameter, a (Åm)	Unit cell volume, $V (\times 10^{-29}$ m³)	Strain, ε' (%)	Stress, σ (GPa)
NSBS1	43.03	0.537	16.62	2.1023	4.2046	7.43	0.66	− 2.12
NSBS2	42.74	0.538	16.58	2.1159	4.2317	7.58	1.31	− 4.22
NSBS3	42.75	0.503	17.73	2.1154	4.2308	7.57	1.29	− 4.15

The results show that all samples exhibit lattice expansion as compared to that of the bulk NiO structure. This lattice expansion occurrence might be an indication that high oxygen atoms have been integrated into the NiO lattice [32]. Note that, nevertheless, the ionic radius of the oxygen ion (0.140 nm) is larger than the ionic radius of Ni^{2+} ion (0.069 nm). The calculation results also show that the values of d and a for the NSBS2 sample were the highest, with values of 2.1159 Å and 4.2317 Å, respectively, followed by NSBS3 and NSBS1. As a result, the unit cell volume (V) of NSBS2 exhibits the highest value as can be calculated from the following formula:

$$V = a^3 \tag{9}$$

The V values for all samples are tabulated in Table 1.

The strain ε values of the samples were estimated using Williamson–Hall plots as shown in Fig. 5a, b, and c corresponding to the NSBS1, NSBS2, and NSBS3 sample, respectively. The Williamson–Hall (W–H) plots were drawn from a following equation [33]:

$$\beta \cos\theta = \frac{0.94\lambda}{D} + 4\varepsilon \sin\theta \tag{10}$$

Here, ε represents induced strain in crystallite, θ denotes the diffraction angle, and D is the average crystallite size. The slope and intercept value of the line fitted to the data points correspond to the strain value and average crystallite size, respectively. The strain value and average crystallite size

Table 2 Crystallite size and strain values of NSBS samples from W–H plot

Sample	Average crystallite size (nm)	Strain, ε
NSBS1	19.28	7.52×10^{-4}
NSBS2	20.47	1.37×10^{-3}
NSBS3	22.19	1.12×10^{-3}

of the NSBS samples are shown in Fig. 5d and tabulated in Table 2.

Subsequently, the strain (ε') and stress (σ) can also be calculated from the values of d and a. The ε' and σ of the samples were analysed by using the following equations:

$$\varepsilon' = \frac{a - a_o}{a_o} \times 100 \tag{11}$$

$$\sigma = \frac{-E(a - a_o)}{2a_o p} \tag{12}$$

Here, a is the lattice parameter of synthesised NiO, $a_o = 4.1771$ Å is the lattice constant of the bulk NiO, $E = 200$ GPa is the Young's modulus for NiO, and $p = 0.31$ is the Poisson ratio for NiO. The strain ε' was also calculated using other formula reported in the literature and the results obtained could provide complementary data to the strain ε calculated from Williamson–Hall plot [23, 34]. For both ε and ε' strain evaluation, if the strain is in a positive value, it is considered as a tensile strain, otherwise, it is considered

Fig. 5 The Williamson–Hall (W–H) plot for **a** NSBS1, **b** NSBS2, and **c** NSBS3 samples. **d** The strain, ε, and average crystallite size of NSBS samples from W–H plot
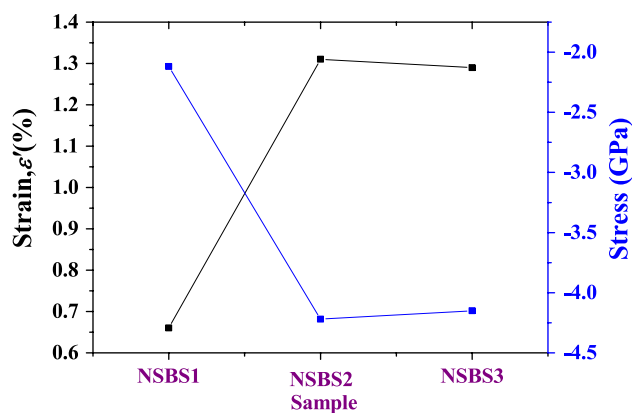
Fig. 6 The strain, ε' and stress of NSBS1, NSBS2, and NSBS3
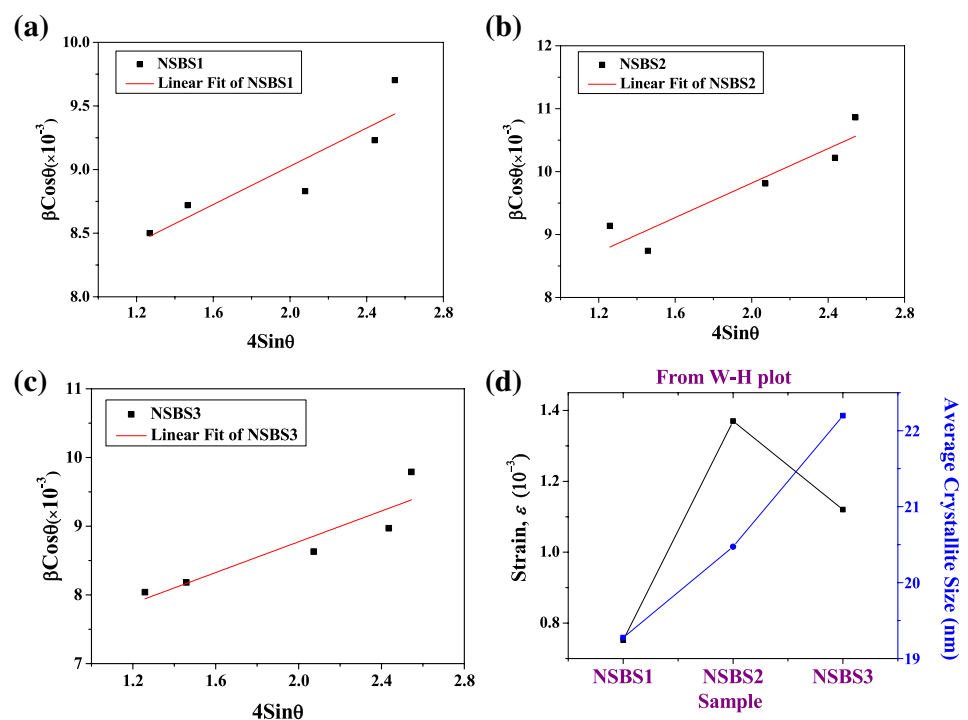
Fig. 7 Transmittance spectra of NSBS1, NSBS2, and NSBS3

as a compressive strain. Meanwhile, for the stress evaluation, if the stress is in a positive value, it is considered as tensile stress, while at negative stress values, it represents a compressive stress [2, 35]. Therefore, the calculated strain and stress presented in Table 1 and in Fig. 6 showed that the all NSBS samples exhibit tensile strain and compressive stress. This can be attributed that the highest values of d, a, and V in the NSBS2 sample causing the percentage of strain to increases in a positive direction (more tensile) and the stress decreases negatively (more compressive). The presence of deficiencies in the crystal's lattice such as grain boundaries, stacking faults, and dislocation possibly contributes to the stress and strain in the films [29]. The grain boundary formations are often considered to generate the stress and strain in the films. The attractive interactions between the grains causes tensile stress, while the addition of an adatom into the grain boundaries causes a compressive stress [36]. Meanwhile, their stress and strain magnitudes are related to an interaction between the atom surface mobility and their growth rate [37]. During the fabrication of nanostructured films using the aqueous solution approach, stresses can occur in the grown films resulting in a lattice strain. The stress and strain are mainly dependent on the growth parameters, and it can exhibit either compressive or tensile or both during the growth process. The increase of stress towards a compressive stress provides an indication of high adsorbed oxygen ions or oxygen interstitial defects in the NSBS2 sample, which commonly occurs for the growth in an oxygen-rich environment such as the growth in the aqueous-based method. The formation of adsorbed oxygen ions, or interstitial oxygen defects, could be described by the following equation:

$$\frac{1}{2}O_2 + 2NiO \longrightarrow O''_{surf} (or \cdot O''_i) + 2Ni^{\bullet}_{Ni} + 2O^{\times}_O \tag{13}$$
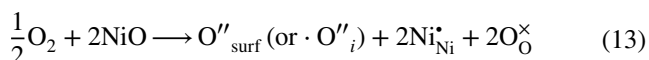
According to several literature reports, these adsorbed oxygen ions or oxygen interstitials could increase the $Ni^{3+}/$ Ni^{2+} ratio by the ox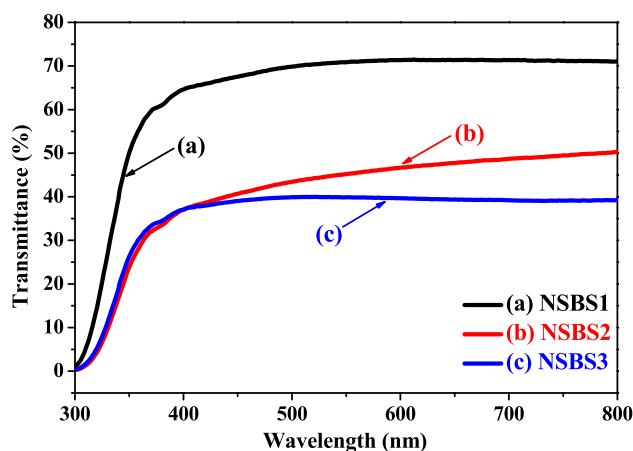idation process of Ni^{2+} ion in NiO into Ni^{3+} [9, 38]. During the growth processes of the NSBS, incidence of structural defects, which include broken bonds, dislocations, and nonstoichiometric composition, could be generated at the grain boundaries. These defects might facilitate intrinsic stresses in the NSBS, which produces compressive stress and tensile strain in the NSBS samples. This result suggests that the NSBS2 sample exhibits higher structural defects compared to the other samples.

3.3 Optical properties

The changes in the lattice properties as shown by the XRD results may contribute to the changes in the optical properties. As shown in Fig. 7, the transmittance spectra for NSBS samples were measured in the wavelength range between 300 and 800 nm. The transmittance of light is relatively high in the visible region but drops rapidly when the wavelength reaches the UV region below 400 nm. From the glimpse of the transmittance spectra, the highest transparency in the visible region (400–800 nm) was identified for NSBS1. This value may be due to the thinness of the NSBS1 structure, which can be seen in the cross-sectional image of FESEM. Therefore, it allows the incident light to easily penetrate the NSBS1 sample. The second highest transparency was recorded for the NSBS2 sample, while the NSBS3 sample showed the lowest transparency value. The reduction of transparency for the NSBS2 and NSBS3 samples may be closely related to the high density of the NiO nanosheet and the hierarchical nanoball-flower-like structures for NSBS2 and NSBS3 samples, as can be viewed from the cross-sectional FESEM images in Fig. 2a–c. Therefore, the loss of penetrated light could be due to light scattering as it travels into the NSBS samples [39]. In addition, the NSBS2 and NSBS3 samples might have higher oxygen interstitial defects, as shown by superior lattice expansion

Table 3 The average transmittance in the visible region and optical bandgap of NSBS samples

Sample	Transmittance (%)	Optical bandgap (E_g)
NSBS1	70	3.75
NSBS2	46	3.72
NSBS3	39	3.73
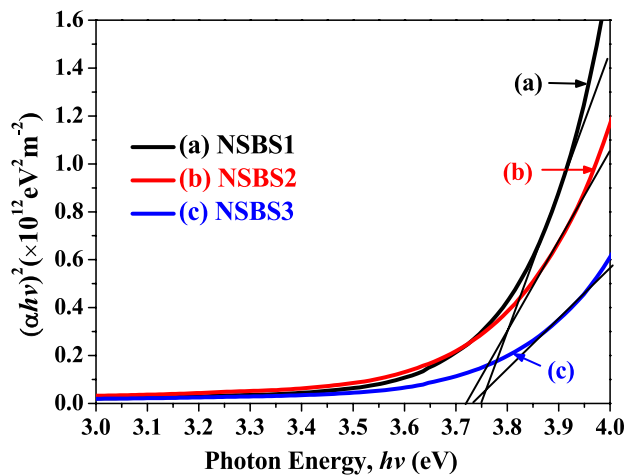
Fig. 8 The Tauc plot for estimation of optical bandgap energy, E_g for NSBS samples

in the XRD result, which causes the defect scattering of light and reduces the light transmission that passes through the samples [32]. The average transmittance values in the visible spectral region (400–800 nm) were estimated to be approximately 70%, 46%, and 39% for NSBS1, NSBS2, and NSBS3 samples, respectively. These values are summarised in Table 3.

Referring to the Tauc plot of $(\alpha h\nu)^2$ versus photon energy $(h\nu)$ in Fig. 8, the optical bandgap energies (E_g) of the NSBS1, NSBS2, and NSBS3 were estimated. The E_g can be determined by obtaining the $h\nu$ value, found by extrapolating the linear curve and noting the intercept with the x-axis. The E_g in the high absorption region could be expressed by the following Tauc relation:

$$\alpha h\nu = B\left(h\nu - E_g\right)^n \tag{14}$$

where α is the absorption coefficient, $h\nu$ is the photon energy, E_g is the optical bandgap, B is an energy-independent constant (1×10^5 to 1×10^6 cm^{-1}eV^{-1}) which is dependent on the electron–hole mobility, and $n = \frac{1}{2}$ is used for directly allowed transitions. The acquired optical bandgap values are summarised in Table 3 and estimated at 3.75, 3.72, and 3.73 eV for the NSBS1, NSBS2, and NSBS3 samples, respectively. According to this analysis, the calculated

bandgap energy values of the samples follow this order NSBS2 < NSBS3 < NSBS1. This ordering also imitates the lattice expansion as discussed in the XRD results. Therefore, the disparity in the bandgap values results from the variation in structural parameters as discussed in the XRD analysis. A lower bandgap energy value is normally produced in the film that has a higher tensile strain or compressive stress [40]. Meanwhile, a higher bandgap energy will be induced in the film if it has a higher compressive strain or tensile stress. In addition, the lattice expansion also influences the bandgap energy of the film. The lattice expansion provides a lower band gap because it lessens the repulsion between the Ni 3d and O 2p orbitals. These findings agree with the reported results in the literature [23, 32]. In addition, the variation in bandgap energy could be attributed to the agglomeration of particles and formation of big clusters in the films as reported by other researchers [41–43]. The variation of the bandgap energy value might also be associated to the correlation energies between the electrons and holes and the existence of defects in the quasi-particle systems [44]. It is noteworthy, that the decrease in E_g for the NSBS2 and NSBS3 samples could be related to the transitions that happen in NiO. The interstitial oxygen in the lattice could create defects in the NSBS and thus engender extra energy states between the valence band and the conduction band. Subsequently, it lowers the bandgap energy value due to the defect state interactions [45].

3.4 Current–voltage analysis

In order to investigate the electrical properties of the NSBS1, NSBS2, and NSBS3, the current–voltage (I–V) using a two-probe measurement was performed at room temperature. The I–V plot with a bias range of − 10 to 10 V, as shown in Fig. 9a–c, indicates the ohmic behaviour for all the samples. The linear plot at the current signal obeys Ohm's law with the current passing through the material being directly proportional to the voltage. Based on the I–V plots, it can be seen that the highest current at the respective voltage was recorded for the NSBS2 sample with the lowest resistance value of 7.84 MΩ. The resistances of the NSBS1 and NSBS3 samples are 9.42 and 8.74 MΩ, respectively, which were determined from the graph via Ohm's law ($V = IR$). The resistance values for the synthesised samples ware summarised in Fig. 9d.

3.5 Humidity sensing performance

The changes in the current signal of the NSBS samples as a function of relative humidity (RH) level are shown in Fig. 10. The measurement was performed for a complete cycle from an initial RH level of 40% to 90% RH, and subsequently back to the initial value of 40% RH again.

Fig. 9 I–V measurement plot for **a** NSBS1, **b** NSBS2, and **c** NSBS3 samples. **d** The resistance plot of the NSBS samples
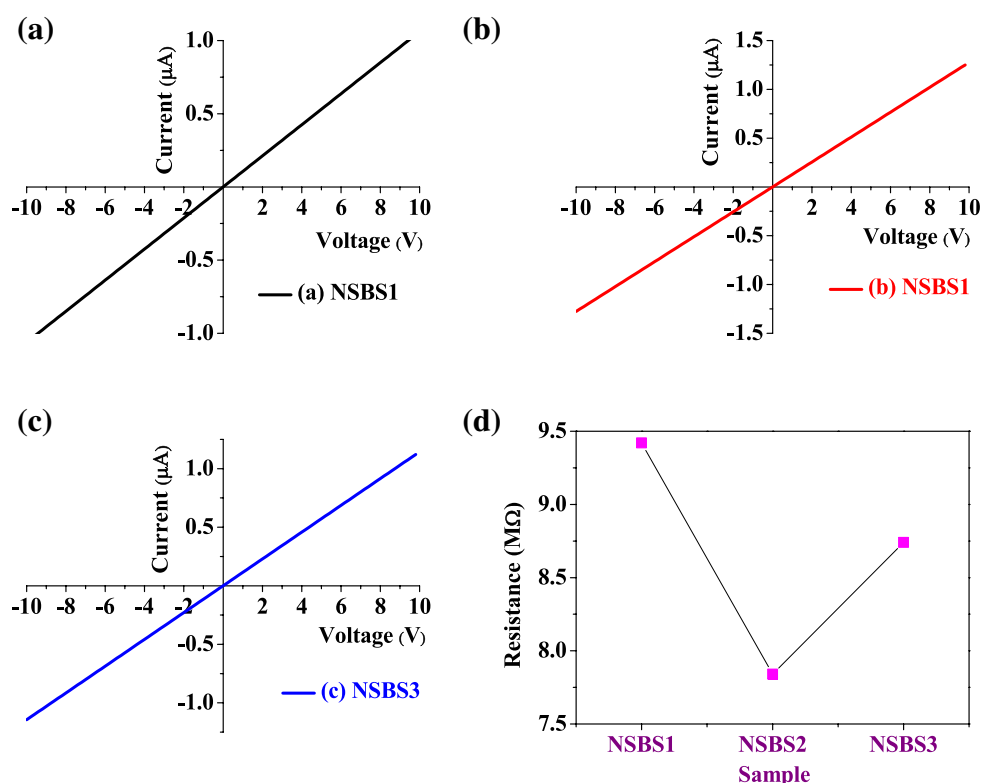
During the measurement, the humidity chamber was set at room temperature of 25 °C while a voltage source of 5 V was applied across the two Ag electrodes. Based on the results, it can be observed that all NSBS samples yielded the same pattern of current responses with the exponential curves, but with different current values. Primarily, the measurement results show a stable current value at an initial level of 40% RH and the current increases rapidly when the humidity increases to 90% RH. Subsequently, the value of the current decreases gradually as the humidity level reduces back to initial value of 40% RH. The

sensitivity (*S*) of the sensor device was calculated using the following equation [46]:

$$S = \frac{R_{40}}{R_{90}} \tag{15}$$

where R_{90} is the resistance at 90% RH and R_{40} is the resistance at 40% RH. The results revealed that the NSBS2 sample shows the highest sensitivity of 169. Meanwhile, the NSBS1-based sensor shows the lowest sensitivity of 110, while the NSBS3 recorded a sensitivity value of 129. The highest sensitivity generated by the NSBS2 can be attributed to the highest current produced at 90% RH, compared to that of other samples. Kennedy et al. [47] stated that the high response of the humidity sensor is due to the high surface area where it facilitates water molecules to adsorb more at the active sites through the chemisorption and physisorption processes. Ismail et al. [39] explained that the wide pore channels in the structures will lead to the improved sensitivity of humidity sensing.

Furthermore, the stability of the NSBS2 sample, which recorded the highest sensitivity value, was tested for several cycles and at different humidity levels. Figure 11 shows the humidity response of NSBS2 for five cycles. The humidity response was measured to confirm the stability of the NSBS2 at various cycles. It can be observed that the NSBS2 showed a very stable response as the curves
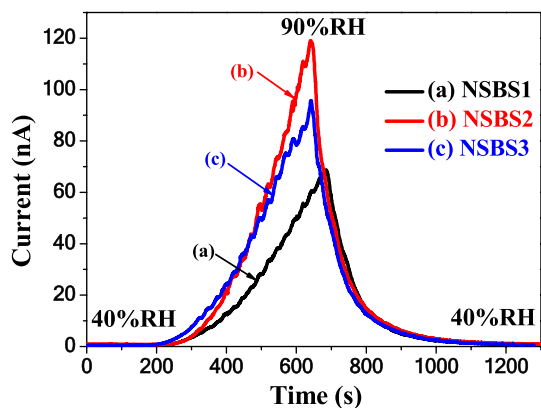

Fig. 10 Humidity sensor responses of nanoball-flower-like NiO at different immersion hours with a bias voltage of 5 V
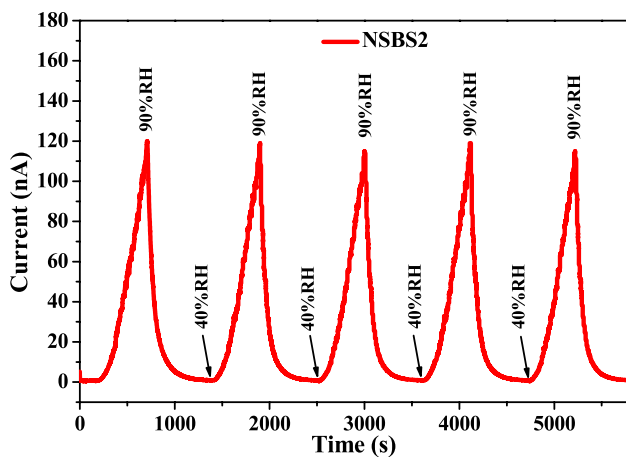
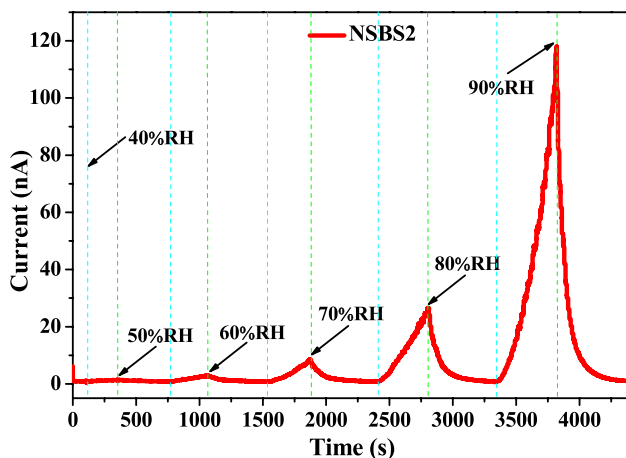**Fig. 11** Five cycles of humidity sensing response at NSBS2 sample

Fig. 12 Humidity sensing response of NSBS2 at different levels of relative humidity

produced are nearly of identical shape and height for all cycles.

Figure 12 depicts the humidity sensing response of NSBS2 at five relative humidity (RH) levels ranging from 50 to 90% RH. The sensitivities of 50%, 60%, 70%, 80%, and 90% RH are 1.4, 2.7, 8.3, 25.5, and 169, respectively. This result indicates that the NSBS2 is sensitive to the different levels of RH. Moreover, it can be seen that its sensitivity increases with the increase of RH levels.

Generally, the performance of the humidity sensor is largely dependent on the surface availability. The large surface area, large surface-to-volume ratio, and small grain size of the prepared materials have been reported to be the reasons on the good sensing performance obtained [48–50]. The availability of a large surface area stimulates water vapour dispersion and expedites the adsorption of water molecules during sensing activities [51, 52]. Besides, the morphology of NSBS plays an important role in enhancing the humidity

response because its high surface area facilitates more adsorption and desorption of water vapour effectively on the NSBS surfaces. From the FESEM images in Figs. 2a and 1b, it is obvious that the NSBS2 sample possesses a larger surface area compare to NSBS1 due to its higher density of NiO nanoball-flower-like structures and thicker NiO nanosheet arrays. The larger the surface area, the larger the water molecules could be adsorbed on the film. Hence, a higher density of charge carriers could be generated in NSBS2, which results in a high current and improved sensitivity values. However, the current and sensitivity values of the NSBS3 sample decreased, although it does have a higher density of NiO nanoball-flower-like structures compared to the other samples. We believe that the resistance of the NSBS samples affects the humidity sensing performance as characterised by the I–V measurement. The resistance of the NSBS3 sample is higher compared to NSBS2 sample which may be due to grain boundary scattering induced by a high density of NiO nanoball-flower-like structures that obstruct the movement of free charge carriers. This carrier scattering effect occurs at the grain boundaries, which results in a decreased sensing performance, as also reported by other researchers [53]. The increase in the density of the NiO nanoball-flower-like structures in the NSBS3 sample induce excessive grain boundaries, resulting in the generation of higher interfacial states between the NiO nanoball-flower-like structures with one another and subsequently produces poor carrier transport properties in the NSBS3 sample [54]. Furthermore, the surface morphology of NSBS3 showed a slight deterioration compared to the other samples, as discussed previously, which might contribute to the slight decline in the humidity sensing performance. Therefore, the generated current during humidity exposure to a high level up to 90% RH, reduced slightly for NSBS3, and produced a lower sensitivity value than that of the NSBS2 sample.

It has been reported that high tensile strain produced in the material resulted in a high ionic conductivity of the material [55, 56]. The ionic conduction is one of the important mechanisms in the humidity sensing, which is discussed later. Therefore, the high tensile strain in the NiO lattice could contribute to the high ionic conductivity in the film during NSBS exposure to humidity. The high tensile strain may result in a decrease of the migration activation energy of the hydronium ions. Therefore, the ions could move freely at high density in the film that has a high tensile strain. From the XRD analysis, the NSBS2 exhibits the highest tensile strain, which could explain the highest current value recorded in the humidity plot in Fig. 10, compared to the other samples, when the humidity level reach 90% RH. This trend of current level was followed by NSBS3 and NSBS1, which follows the trend of the tensile strain values calculated in the XRD analysis.

In addition, the carrier concentration and carrier mobility of the samples also contribute to the performance of the humidity sensing. It has been reported that the carrier type and carrier concentration of the materials play important role in the sensing mechanism and sensing performance [57, 58]. The improvement in hole concentration also improved the ionic conductivity, as previously reported [59]. Therefore, the Hall effect measurements were conducted on NSBS1 and NSBS3, which have the lowest and the highest current response at 90% RH. From the measurement, both samples exhibited p-type semiconductor behaviour. Therefore, the carrier concentration and mobility are of the hole carrier type for the NSBS samples. The sheet resistances were measured for the NSBS1 and NSBS2 samples with values of 1.17×10^5 and 5.44×10^4 Ω/sq., respectively. The hole carrier concentration for the NSBS2 sample (8.71×10^{15} hole/cm^{-3}) was greater than the hole carrier concentration for the NSBS1 sample (6.11×10^{15} hole/cm^{-3}). In addition, the hole mobility in the NSBS2 was 1.88×10^2 cm^2/V s, which is larger than that of the NSBS1 sample with a value of 6.1×10^1 cm^2/V s. Generally, nonstoichiometric NiO is recognised to have hole conductivity due to the excessive amount of ionised Ni^{2+} cationic vacancies and oxygen interstitial defects [60]. The defect in the lattice is crucial for the sensing mechanism and plays important role to control the reaction rate of the sensor [61]. Based on the Hall measurement results, it indicates that the NSBS2 sample has a higher number of Ni^{2+} cationic vacancies and oxygen interstitial defects than the NSBS1 sample, which produced the higher p-type conductivity of the NSBS2 sample compared to the NSBS1 sample. It also reinforces that the NSBS2 sample has a higher Ni^{3+}/Ni^{2+} ratio than the NSBS1 sample. The relationship between the Ni^{2+} cationic vacancies, oxygen interstitial defects, and Ni^{3+} in the NiO lattice can be expressed by the following equation [1]:

$$\frac{1}{2}O_2 + 2Ni_{Ni}^{X} \rightarrow 2Ni_{Ni}^{\bullet} + O_O^{\times} + V''_{Ni} \tag{16}$$
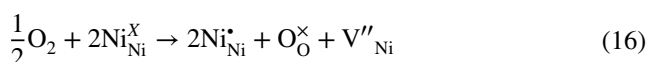
where Ni_{Ni}^{X} represents Ni^{2+} ions at the lattice, $Ni_{Ni}^{\bullet}$ is the Ni^{3+} ions at Ni^{2+} site, $O_O^{\times}$ represents O^{2-} ion at the lattice, and V''_{Ni} denotes the Ni^{2+} cationic vacancy. The generated Ni^{3+} ions are acceptors, which influence the electrical properties of the NiO. Thus, a higher hole concentration is generated in the NSBS2 when higher Ni^{2+} cationic vacancies and Ni^{3+} ions are created in the sample [62]. The Ni^{3+} ions are reported to facilitate the sites for chemisorption of the hydroxyl groups, which plays an important role in the humidity sensing mechanism [63]. This result confirmed the XRD and optical results as discussed earlier. These results also indicate that the NSBS2 sample is a good p-type NiO, which has a low sheet resistance value as a result of its high hole carrier concentration and hole mobility. Therefore, we believe that the low sheet resistance of the films also plays

an important role to improve the current response of the humidity sensor.

Generally, the humidity sensing mechanism for this humidity sensor can be described in several stages. At an initial stage of low relative humidity (RH), the quantity of water molecules available in atmosphere is very small. These water molecules are adsorbed and chemically react with the NSBS surface and form a chemisorbed monolayer. The attraction of water molecules was induced by the electrostatic interaction between Ni^{3+} or Ni^{2+} and OH$^-$ ions. When the environment gets more humid, another layer of the water molecules is physically adsorbed on the chemisorbed monolayer. This condition is known as the physisorbed layer due to the formation of hydrogen bonds (chemisorbed OH$^-$ layer and the oxygen atom of water molecules). The water molecules from the physisorbed layer are then decomposed into H$_3$O$^+$ and OH$^-$ ions because of the high electrostatic field on the top of the NSBS surface. The positive charge (H$^+$) from the hydronium ion (H$_3$O$^+$) jumps from one water molecule to another continuously and becomes the source of electrical conduction. The H$^+$ ions could hop or tunnel from one water molecule to another water molecule due to the high mobility of the proton in the water vapour. The conduction occurs by H$^+$ ions in the surface of the aqueous layer. This hopping incidence is called proton hopping and the mechanism is known as the Grotthuss chain. Thus, at this stage, the current signal of the humidity sensor increases due to the protonic conduction. The reaction at the physisorbed water layer as described by the Grotthuss chain can be shown as follows [64]:

$$2H_2O \rightarrow H_3O^+ + OH^- \tag{17}$$

$$H_3O^+ \rightarrow H_2O + H^+ \tag{18}$$

At the stage of high RH level, the thickness of the physisorbed water layer increases and the reaction processes happen at a higher rate. Thus, more H$^+$ ions are generated at this stage to contribute a higher current signal due to the protonic conduction. At the very high humidity stage, huge amounts of water molecules are adsorbed in the crevices between the NSBS which induces capillary condensation [65]. At the same time, electrolytic conduction occurs simultaneously with the protonic conduction and attains an equilibrium state. During this stage, charge transport increases significantly to produce more current signals. As a result, the conductivity of the NSBS is enhanced significantly. The conduction mechanism of humidity sensing for the NSBS samples is illustrated in Fig. 13.
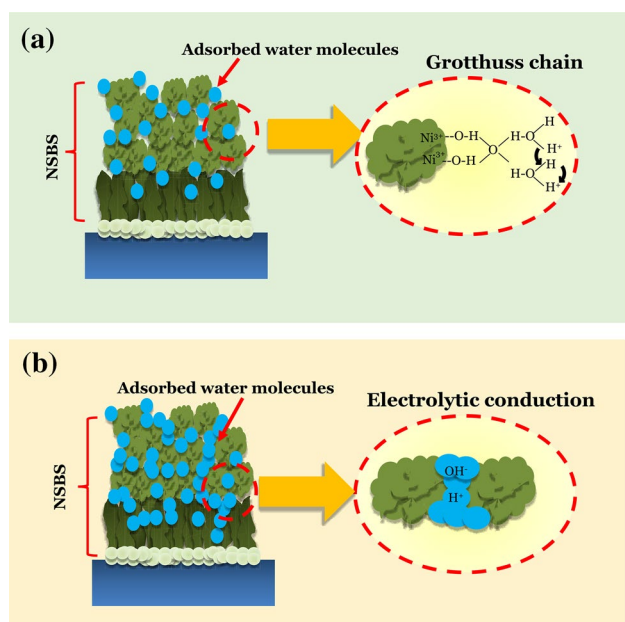
Fig. 13 The sensing mechanism of the NSBS based on **a** ionic conduction at low humidity level and **b** electrolytic conduction at high humidity level

4 Conclusion

The growth of NSBS1, NSBS2, and NSBS3 samples on NiO seed-coated glass substrates was accomplished using a low-temperature immersion method. The grown NSBS samples were highly porous and their surfaces exhibited hollow structures with the presence of fine holes in a thin network series consisting of granular NiO nanoparticle structures. The nanoball-flower-like NiO, grown in the NSBS1–NSBS3 samples, has diameter between 1.5 and 3.3 μm. The XRD patterns showed that all the NSBS samples have polycrystalline structures that corresponded to the face-centred cubic NiO. There are five diffraction peaks observed in the XRD patterns, which were indexed to (111), (200), (220), (311), and (222) planes. The lattice parameters d and a for the NSBS2 sample were the highest, with values of 2.1159 Å and 4.2317 Å, respectively, followed by NSBS1 (d: 2.1023 Å, a: 4.2046 Å) and NSBS3 (d: 2.1154 Å, a: 4.2308 Å). As a consequence, this condition causes the NSBS2 sample to have a higher tensile strain and compressive stress than other samples, with values of -4.22 GPa and 1.31%, respectively. The optical bandgap energy values for NSBS1, NSBS2, and NSBS3 samples were 3.75, 3.72, and 3.73 eV, respectively. The calculated bandgap energy values with NSBS2 < NSBS3 < NSBS1 correlated to the lattice expansion discussed in the XRD results. The I–V measurement results showed that the NSBS2 sample exhibited the lowest resistance value of 7.84 MΩ. The humidity sensing results revealed that the NSBS2 sample shows the highest

sensitivity of 169 due to its excellent structural and electrical characteristics such as high lattice tensile strain, enormous surface area, low resistance, high hole carrier concentration, and hole mobility. In addition, NSBS3 also showed a good repeatability performance and sensitivity to different humidity levels, ranging from 40 to 90% RH.

References

1. P. Yang, L. Li, S. Yu, H. Zheng, W. Peng, The annealing temperature and films thickness effect on the surface morphology, preferential orientation and dielectric property of NiO films. Appl. Surf. Sci. **493**, 396–403 (2019)
2. M.H. Mamat, N. Parimon, A.S. Ismail, I.B. Shameem Banu, S. Sathik Basha, G.V. Vijayaraghavan, M.K. Yaakob, A.B. Suriani, M.K. Ahmad, M. Rusop, Structural, optical, and electrical evolution of sol–gel-immersion grown nickel oxide nanosheet array films on aluminium doping. J. Mater. Sci.: Mater. Electron. **30**, 9916–9930 (2019)
3. Y. Qin, J. Song, Q. Qiu, Y. Liu, Y. Zhao, L. Zhu, Y. Qiang, High-quality NiO thin film by low-temperature spray combustion method for perovskite solar cells. J. Alloy. Compd. **810**, 151970 (2019)
4. G. Li, K. Deng, Y. Dou, Y. Liao, D. Wang, J. Wu, Z. Lan, Self-assembled NiO microspheres for efficient inverted mesoscopic perovskite solar cells. Sol. Energy **193**, 111–117 (2019)
5. Y. Liu, J. Song, Y. Qin, Q. Qiu, Y. Zhao, L. Zhu, Y. Qiang, Cu-doped nickel oxide hole transporting layer via efficient low-temperature spraying combustion method for perovskite solar cells. J. Mater. Sci.: Mater. Electron. **30**, 15627–15635 (2019)
6. X. Shi, S. Zhang, X. Chen, T. Tang, R. Klingeler, E. Mijowska, Ultrathin NiO confined within hollow carbon spheres for efficient electrochemical energy storage. J. Alloy. Compd. **797**, 702–709 (2019)
7. J.H. Oh, M. Su Jo, S.M. Jeong, C. Cho, Y.C. Kang, J.S. Cho, New synthesis strategy for hollow NiO nanofibres with interstitial nanovoids prepared via electrospinning using camphene for anodes of lithium-ion batteries. J. Ind. Eng. Chem. **77**, 76–82 (2019)
8. S. Saffarzadeh, G. Nabiyouni, F. Heidary, A short time microwave method for synthesis of magnetic NiFe$_2$O$_4$/NiO nanocomposites as a clean technology in photocatalytic degradation of water pollutants. J. Mater. Sci.: Mater. Electron. **30**, 8171–8181 (2019)
9. M. ul Haq, Z. Zhang, Z. Wen, S. Khan, S. ud Din, N. Rahman, L. Zhu, Humidity sensor based on mesoporous Al-doped NiO ultralong nanowires with enhanced ethanol sensing performance. J. Mater. Sci.: Mater. Electron. **30**, 7121–7134 (2019)
10. H. Yin, T. Zhan, J. Chen, L. Wang, J. Gong, S. Zhao, Z. Ji, Q. Nie, Polyhedral NiO/C porous composites derived by controlled pyrolysis of Ni-MOF for highly efficient non-enzymatic glucose detection. J. Mater. Sci.: Mater. Electron. **31**, 4323–4335 (2020)
11. X. San, G. Wang, B. Liang, J. Ma, D. Meng, Y. Shen, Flower-like NiO hierarchical microspheres self-assembled with nanosheets: surfactant-free solvothermal synthesis and their gas sensing properties. J. Alloy. Compd. **636**, 357–362 (2015)

12. H. Zhang, W.G. Chen, Y.Q. Li, L.F. Jin, F. Cui, Z.H. Song, 3D flower-like NiO hierarchical structures assembled with size-controllable 1D blocking units: gas sensing performances towards acetylene. Front Chem 6, 472 (2018)

13. J. Wang, W. Zeng, Z. Wang, Assembly of 2D nanosheets into 3D flower-like NiO: synthesis and the influence of petal thickness on gas-sensing properties. Ceram. Int. 42, 4567–4573 (2016)

14. G. Singh, R.C. Singh, Highly sensitive and selective liquefied petroleum gas sensor based on novel ZnO–NiO heterostructures. J. Mater. Sci.: Mater. Electron. 30, 20010–20018 (2019)

15. H. Farahani, R. Wagiran, M.N. Hamidon, Humidity sensors principle, mechanism, and fabrication technologies: a comprehensive review. Sensors 14, 7881–7939 (2014)

16. M.H. Mamat, N. Parimon, M.A.R. Abdullah, A.S. Ismail, M.F. Malek, W.R.W. Ahmad, A.S. Zoolfakar, A.B. Suriani, M.K. Ahmad, N. Nayan, I.B. Shameem Banu, R. Amiruddin, M. Rusop, Fabrication of nickel oxide nanowall network films at different annealing temperatures for humidity sensing applications. Int. J. Eng. Technol. 7, 277–282 (2018)

17. Y.-B. Li, Y.-P. Liu, J. Wang, Y.-L. Guo, K. Chu, Plasma-engineered NiO nanosheets with enriched oxygen vacancies for enhanced electrocatalytic nitrogen fixation. Inorg. Chem. Front. 7, 455–463 (2020)

18. C. Feng, Z. Jiang, B. Chen, P. Cheng, Y. Wang, C. Huang, Aluminium-doped NiO nanofibres as chemical sensors for selective and sensitive methanol detection. Anal. Methods 11, 575–581 (2019)

19. U.T. Nakate, R. Ahmad, P. Patil, Y.T. Yu, Y.-B. Hahn, Ultra thin NiO nanosheets for high performance hydrogen gas sensor device. Appl. Surf. Sci. 506, 144971 (2020)

20. Y. Wang, Y. Chen, J. Wang, X. Xv, X. Yang, J. Zhou, S. Li, F. Cao, G. Qin, Novel porous ultrathin NiO nanosheets for highly efficient water vapour adsorption-desorption. Sep. Purif. Technol. 226, 299–303 (2019)

21. J. Rouhi, M.H. Mamat, C.H.R. Ooi, S. Mahmud, M.R. Mahmood, High-performance dye-sensitised solar cells based on morphology-controllable synthesis of ZnO–ZnS heterostructure nanocone photoanodes. PLoS ONE 10, e0123433 (2015)

22. M. Alimanesh, Z. Hassan, N. Zainal, Electrochemical growth of controlled tip shapes of ZnO nanorod arrays on silicon substrate and enhanced photoluminescence emission from nanopyramid arrays compared with flat-head nanorods. Opt. Mater. 72, 276–282 (2017)

23. M.H. Mamat, N. Parimon, A.S. Ismail, I.B. Shameem Banu, S. Sathik Basha, R.A. Rani, A.S. Zoolfakar, M.F. Malek, A.B. Suriani, M.K. Ahmad, M. Rusop, Synthesis, structural and optical properties of mesostructured, X-doped NiO (x = Zn, Sn, Fe) nanoflake network films. Mater. Res. Bull. 127, 110860 (2020)

24. H. Jiang, T. Zhao, C. Li, J. Ma, Hierarchical self-assembly of ultrathin nickel hydroxide nanoflakes for high-performance supercapacitors. J. Mater. Chem. 21, 3818–3823 (2011)

25. S.K. Meher, P. Justin, G. Ranga Rao, Nanoscale morphology dependent pseudocapacitance of NiO: influence of intercalating anions during synthesis. Nanoscale 3, 683–692 (2011)

26. S.K. Meher, P. Justin, G. Ranga Rao, Microwave-mediated synthesis for improved morphology and pseudocapacitance performance of nickel oxide. ACS Appl. Mater. Interfaces. 3, 2063–2073 (2011)

27. M.H. Mamat, M.F. Malek, N.N. Hafizah, M.N. Asiah, A.B. Suriani, A. Mohamed, N. Nafarizal, M.K. Ahmad, M. Rusop, Effect of oxygen flow rate on the ultraviolet sensing properties of zinc oxide nanocolumn arrays grown by radio frequency magnetron sputtering. Ceram. Int. 42, 4107–4119 (2016)

28. Y. Li, M. Guo, M. Zhang, X. Wang, Hydrothermal synthesis and characterisation of TiO_2 nanorod arrays on glass substrates. Mater. Res. Bull. 44, 1232–1237 (2009)

29. A. Jafari, K. Tahani, D. Dastan, S. Asgary, Z. Shi, X.-T. Yin, W.-D. Zhou, H. Garmestani, Ş. Ţălu, Ion implantation of copper oxide thin films; statistical and experimental results. Surf. Interfaces 18, 100463 (2020)

30. D. Dastan, N. Chaure, M. Kartha, Surfactants assisted solvothermal derived titania nanoparticles: synthesis and simulation. J. Mater. Sci.: Mater. Electron. 28, 7784–7796 (2017)

31. D. Dastan, Effect of preparation methods on the properties of titania nanoparticles: solvothermal versus sol–gel. Appl. Phys. A 123, 699 (2017)

32. J.D. Hwang, T.H. Ho, Effects of oxygen content on the structural, optical, and electrical properties of NiO films fabricated by radio-frequency magnetron sputtering. Mater. Sci. Semicond. Process. 71, 396–400 (2017)

33. P.E. Saranya, S. Selladurai, Mesoporous 3D network Ce-doped NiO nanoflakes as high performance electrodes for supercapacitor applications. New J. Chem. 43, 7441–7456 (2019)

34. R. Barir, B. Benhaoua, S. Benhamida, A. Rahal, T. Sahraoui, R. Gheriani, Effect of precursor concentration on structural optical and electrical properties of NiO thin films prepared by spray pyrolysis. J. Nanomater. 2017, 5204639 (2017)

35. A.S. Ismail, M.H. Mamat, M.F. Malek, M.M. Yusoff, R. Mohamed, N.D.M. Sin, A.B. Suriani, M. Rusop, Heterogeneous SnO_2/ZnO nanoparticulate film: facile synthesis and humidity sensing capability. Mater. Sci. Semicond. Process. 81, 127–138 (2018)

36. E. Chason, P.R. Guduru, Tutorial: understanding residual stress in polycrystalline thin films through real-time measurements and physical models. J. Appl. Phys. 119, 191101 (2016)

37. E. Chason, A kinetic analysis of residual stress evolution in polycrystalline thin films. Thin Solid Films 526, 1–14 (2012)

38. B.-Y. Kim, J.-W. Yoon, J.K. Kim, Y.C. Kang, J.-H. Lee, Dual role of multiroom-structured Sn-doped NiO microspheres for ultrasensitive and highly selective detection of xylene. ACS Appl. Mater. Interfaces. 10, 16605–16612 (2018)

39. M.A.R. Abdullah, M.H. Mamat, A.S. Ismail, M.F. Malek, A.B. Suriani, M.K. Ahmad, I.B. Shameem Banu, R. Amiruddin, M. Rusop, Direct and seedless growth of Nickel Oxide nanosheet architectures on ITO using a novel solution immersion method. Mater. Lett. 236, 460–464 (2019)

40. M.F. Malek, M.H. Mamat, M.Z. Musa, T. Soga, S.A. Rahman, S.A.H. Alrokayan, H.A. Khan, M. Rusop, Metamorphosis of strain/stress on optical band gap energy of ZAO thin films via manipulation of thermal annealing process. J. Lumin. 160, 165–175 (2015)

41. D. Dastan, N.B. Chaure, Influence of surfactants on TiO_2 nanoparticles grown by sol-gel technique. Int. J. Mater. Mech. Manuf. 2, 21–24 (2014)

42. D. Dastan, Nanostructured anatase titania thin films prepared by sol-gel dip coating technique. J. Atom. Mol. Condens. Nano Phys. 2, 109–114 (2015)

43. D. Dastan, S.L. Panahi, N.B. Chaure, Characterization of titania thin films grown by dip-coating technique. J. Mater. Sci.: Mater. Electron. 27, 12291–12296 (2016)

44. N.-N. Ge, C.-H. Gong, X.-C. Yuan, H.-Z. Zeng, X.-H. Wei, Effect of Mn doping on electroforming and threshold voltages of bipolar resistive switching in Al/Mn: NiO/ITO. RSC Adv. 8, 29499–29504 (2018)

45. R. Sharma, A.D. Acharya, S.B. Shrivastava, M.M. Patidar, M. Gangrade, T. Shripathi, V. Ganesan, Studies on the structure optical and electrical properties of Zn-doped NiO thin films grown by spray pyrolysis. Optik 127, 4661–4668 (2016)

46. N.D. Md Sin, M.H. Mamat, M.F. Malek, M. Rusop, Fabrication of nanocubic ZnO/SnO_2 film-based humidity sensor with high sensitivity by ultrasonic-assisted solution growth method at different Zn:Sn precursor ratios. Appl. Nanosci. 4, 829–838 (2014)

47. L. John Kennedy, P. Magesan, J. Judith Vijaya, M.J. Umapathy, U. Aruldoss, Biominerals doped nanocrystalline nickel oxide as efficient humidity sensor: a green approach. Mater. Sci. Eng. B: Solid-State Mater. Adv. Technol. **190**, 13–20 (2014)

48. X.-T. Yin, W.-D. Zhou, J. Li, Q. Wang, F.-Y. Wu, D. Dastan, D. Wang, H. Garmestani, X.-M. Wang, Ş. Ţălu, A highly sensitivity and selectivity Pt-SnO_2 nanoparticles for sensing applications at extremely low level hydrogen gas detection. J. Alloy. Compd. **805**, 229–236 (2019)

49. X.-T. Yin, P. Lv, J. Li, A. Jafari, F.-Y. Wu, Q. Wang, D. Dastan, Z. Shi, S. Yu, H. Garmestani, Nanostructured tungsten trioxide prepared at various growth temperatures for sensing applications. J. Alloy. Compd. **825**, 154105 (2020)

50. M.H. Mamat, N.N. Hafizah, M. Rusop, Fabrication of thin, dense and small-diameter zinc oxide nanorod array-based ultraviolet photoconductive sensors with high sensitivity by catalyst-free radio frequency magnetron sputtering. Mater. Lett. **93**, 215–218 (2013)

51. A.S. Ismail, M.H. Mamat, I.B. Shameem Banu, M.F. Malek, M.M. Yusoff, R. Mohamed, W.R.W. Ahmad, M.A.R. Abdullah, N.D. Md. Sin, A.B. Suriani, M.K. Ahmad, M. Rusop, Modulation of Sn concentration in ZnO nanorod array: intensification on the conductivity and humidity sensing properties. J. Mater. Sci.: Mater. Electron. **29**, 12076–12088 (2018)

52. A.S. Ismail, M.H. Mamat, M.M. Yusoff, M.F. Malek, A.S. Zoolfakar, R.A. Rani, A.B. Suriani, A. Mohamed, M.K. Ahmad, M. Rusop, Enhanced humidity sensing performance using Sn-doped ZnO nanorod array/SnO_2 nanowire heteronetwork fabricated via two-step solution immersion. Mater. Lett. **210**, 258–262 (2018)

53. J. Zhang, D. Zeng, Q. Zhu, J. Wu, K. Xu, T. Liao, G. Zhang, C. Xie, Effect of grain-boundaries in NiO nanosheet layers room-temperature sensing mechanism under $NO2$. J. Phys. Chem. C **119**, 17930–17939 (2015)

54. I.J. Beyerlein, M.J. Demkowicz, A. Misra, B.P. Uberuaga, Defect-interface interactions. Prog. Mater. Sci. **74**, 125–210 (2015)

55. G.F. Harrington, A. Cavallaro, D.W. McComb, S.J. Skinner, J.A. Kilner, The effects of lattice strain, dislocations, and microstructure on the transport properties of YSZ films. Phys. Chem. Chem. Phys. **19**, 14319–14336 (2017)

56. K. Wen, W. Lv, W. He, Interfacial lattice-strain effects on improving the overall performance of micro-solid oxide fuel cells. J. Mater. Chem. A **3**, 20031–20050 (2015)

57. X.T. Yin, D. Dastan, F.Y. Wu, J. Li, Facile synthesis of SnO_2/ lafeo3 − x nx composite: photocatalytic activity and gas sensing performance. Nanomaterials **9**, 1163 (2019)

58. W.D. Zhou, D. Dastan, J. Li, X.T. Yin, Q. Wang, Discriminable sensing response behavior to homogeneous gases based on n-ZNO/p-NIO composites. Nanomaterials **10**, 785 (2020)

59. M.R. Das, A. Mukherjee, P. Mitra, Influence of Cu incorporation on ionic conductivity and dielectric relaxation mechanism in NiO thin films synthesised by CBD. J. Mater. Sci.: Mater. Electron. **29**, 1216–1231 (2018)

60. S. Dewan, M. Tomar, R.P. Tandon, V. Gupta, Zn doping induced conductivity transformation in NiO films for realisation of p-n homo junction diode. J. Appl. Phys. **121**, 215307 (2017)

61. K. Shan, Z.-Z. Yi, X.-T. Yin, D. Dastan, H. Garmestani, Conductivity and mixed conductivity of a novel dense diffusion barrier and the sensing properties of limiting current oxygen sensors. Dalton Trans. **49**, 6682–6692 (2020)

62. X. Meng, Y. Du, X. Gao, Face–centred cubic p–type NiO films room–temperature prepared via direct-current reactive magnetron sputtering–Influence of sputtering power on microstructure, optical and electrical behaviours. Phys. B **579**, 411897 (2020)

63. S.A. Makhlouf, K.M.S. Khalil, Humidity sensing properties of NiO/Al_2O_3 nanocomposite materials. Solid State Ion. **164**, 97–106 (2003)

64. A.S. Ismail, M.H. Mamat, I.B. Shameem Banu, R. Amiruddin, M.F. Malek, N. Parimon, A.S. Zoolfakar, N.D. Md. Sin, A.B. Suriani, M.K. Ahmad, M. Rusop, Structural modification of ZnO nanorod array through Fe-doping: ramification on UV and humidity sensing properties. Nano-Struct. Nano Objects **18**, 100262 (2019)

65. P.M. Faia, C.S. Furtado, A.J. Ferreira, AC impedance spectroscopy: a new equivalent circuit for titania thick film humidity sensors. Sens. Actuators B: Chem. **107**, 353–359 (2005)